

AMOS Observations of NASA's IMAGE Satellite

Doyle Hall^{1,2}, John Africano^{1,2}, David Archambeault², Brian Birge²,
David Witte³ and Paul Kervin⁴

¹*The Boeing Company, Colorado Springs, CO*

²*Boeing LTS / AMOS, Kihei, HI*

³*Pantera Consulting, Albuquerque, NM*

⁴*Air Force Research Laboratory / Detachment 15, Kihei, HI*

1 SUMMARY

NASA's Imager for Magnetopause-to-Aurora Global Exploration (IMAGE) satellite stopped transmitting telemetry to ground stations in December 2005, after functioning for more than 5 years on Earth orbit. Before this loss of telemetry, the IMAGE satellite actively maintained a spin-stabilized attitude with spin axis perpendicular to the orbital plane and a nominal rotation rate of about 0.5 rpm. The spinning action served to both stabilize the satellite and keep the 250 m-long radial wire antennas of the satellite's Radio Plasma Imager under tension perpendicular to the satellite spin axis. After loss of telemetry, it was unclear whether the spacecraft remained in this spin-stabilized configuration, or whether it could continue to receive and execute up-linked commands. In late January and early February of 2006 the AMOS 3.6m Advanced Electro Optical System (AEOS) conducted an initial set of observations in an effort to help diagnose the state of the unresponsive spacecraft. The AEOS observations employed the Visible Imager (VisIm) instrument in the photometric I-band as well as the long-wavelength infrared (LWIR) imager. The wide field-of-view VisIm images clearly show the long radial wire antennas glinting in reflected sunlight during each revolution of the spinning spacecraft, creating a photometric signature characterized by large amplitude periodic variations. Analysis of concurrent AEOS LWIR observations indicates radiometric temperatures ranging from 250 to 310 Kelvin, with the higher temperatures occurring when more of the continuously-sunlit portions of the spacecraft were observable from AMOS. A detailed periodic analysis of the VisIm photometric signatures acquired on 2006 day-of-year (DOY) 028, 031 and 034 indicates a spin axis orientation consistent with that reported in the last telemetry down-linked from the satellite approximately seven weeks earlier. However, the periodic variations indicate a satellite spin rate of 0.4741 ± 0.0005 rpm, measurably slower than the last known spin rate from down-linked telemetry. Shortly after these initial AEOS observations were conducted, the NASA IMAGE satellite team up-linked commands to the spacecraft to increase the spin rate up to 0.52 rpm in order to test if the spacecraft could receive and execute such commands. Subsequent AMOS observations conducted 2006 DOY 150, however, did not show evidence of an increased spin rate, but instead indicated a further reduction down to 0.4709 ± 0.0004 rpm. The AEOS observations therefore confirm that the IMAGE spacecraft has lost the ability to receive and/or execute up-linked commands, and indicates that, between 2005-DEC-12 and 2006-MAY-30, the spacecraft's spin axis orientation remained stable to within detection limits but the spin rate declined at a rate of $(3.1 \pm 0.3) \times 10^{-5}$ rpm/day, a deceleration most likely caused by magnetically-induced environmental torques.

2 INTRODUCTION

The IMAGE satellite (SSN 26113, 2000-17A) was launched in March 2000, the first of NASA's Medium-class Explorer spacecraft to fly, and was equipped with a payload designed to reveal the workings of Earth's magnetosphere/ionosphere system (see [1, 2] and references therein for a detailed description of the spacecraft and mission). Figure 1 shows a schematic illustration of the spacecraft. Soon after being inserted into an eccentric $1,640\text{km} \times 45,230\text{km} \times 90^\circ$ orbit, the satellite began five highly successful years of mission activity during which it actively maintained a spin-stabilized attitude with the spin axis perpendicular to the orbital plane and a nominal rotation rate of about 0.5 rpm. In addition to stabilizing the spacecraft, this spinning action kept the long radial wire antennas of the satellite's Radio Plasma Imager (RPI) under tension and perpendicular to the satellite spin axis. These four wire antennas were originally 250 m long and gave the newly-deployed spacecraft a remarkable end-to-end equatorial width of 0.5 km.

Although some of these 0.3 mm-diameter antennas suffered loss in length during the extended mission, the RPI experiment and the other components of the satellite's scientific payload returned a tremendous scientific bounty of data via down-linked telemetry.

During December of 2005, after exceeding its original two year design lifetime by more than three years, ground-stations stopped receiving telemetry from the IMAGE spacecraft. The last telemetry from the attitude control system [3] included attitude quaternion vectors spanning the period 2005-Dec-12 06:00-07:38 UT indicating a spin rate of 0.47594 ± 0.00012 rpm and a spin axis orientation with right ascension (RA) of $(291.8 \pm 1.4)^\circ$ and declination (DEC) of $(-0.7 \pm 1.4)^\circ$, within statistical uncertainty of the orbital normal vector. After loss of telemetry, it was unclear whether the spacecraft remained in this spin-stabilized configuration, whether it had entered a "safe" operational mode, or whether it could continue to receive and execute up-linked commands. In order to ascertain these unknowns and further characterize the anomaly, NASA and AMOS agreed to use the AEOS 3.6m telescope to perform observations designed to characterize the status of the spacecraft as much as possible through remote observations.

The first AEOS observations, conducted in late January and early February of 2006, were used to determine the spin state of the spacecraft using time-resolved photometry from the VisIm instrument [5], as well as to measure the figure-averaged temperature using two-band thermal-IR radiometry from the LWIR instrument [6]. The LWIR observations indicated radiometric temperatures in the 250 K to 310 K range, with higher temperatures sensibly corresponding to times when more of the continuously-sunlit portions of the spacecraft were observable from AMOS. However, the LWIR measurements proved difficult for the spacecraft engineering team to use for characterization because of the relatively small expected difference in the thermal signature of the spacecraft in nominal operational mode versus safe mode. Fortunately, the VisIm observations yielded measurements of the spacecraft spin rate with sufficient accuracy to allow a further test if the spacecraft could still execute commands to adjust its spin rate. Soon after the initial AEOS observations, NASA up-linked commands to the spacecraft to increase its spin rate by a detectable amount. Subsequent AEOS VisIm observations conducted in late May 2006 indicated no such spin-up, yielding the conclusion that the IMAGE spacecraft cannot receive and/or execute up-linked commands and is currently passively spinning down on orbit.

3 AEOS VISIM OBSERVATIONS

The data presented in this paper were acquired using the AMOS AEOS 3.6m telescope Visible Imager (VisIm) instrument [7, 8]. The VisIm detector is a Si-based 512×512 pixel cooled Pentamax CCD array, sensitive to light in the 700–1100 nm wavelength range. Although the instrument is equipped with several spectral band-pass filters, all observations for this study employ the Bessel I-band filter which spans the 740–880 nm spectral range, creating a peak photometric response near 790 nm. Observing in the standard astronomical spectral I-band provides the means of establishing an accurate photometric calibration by observing cataloged photometric calibration stars [5, 9]. All observations employed the VisIm $300 \mu\text{rad} \times 300 \mu\text{rad}$ wide field-of-view with exposure times in the 0.25-1.0 second range, but did not use the adaptive optics image compensation capability of the AEOS telescope.

AEOS conducted four observations of the IMAGE satellite on 2006-028, 2006-031, 2006-034, and 2006-150 (dates specified as YEAR-DOY). Many of the wide field-of-view VisIm images clearly show the long radial wire antennas glinting in reflected sunlight as the spacecraft rotates. Figure 2 shows eight selected images from the first AEOS observation (on 2006-028), when the observatory-to-satellite range was between 2,500 and 3,050 km. The eight images show almost two complete rotations of the satellite, each separated by approximately $\frac{1}{4}$ of a rotation period (≈ 30 s). The images clearly show that each radial wire antenna glints in sunlight along its entire length twice per rotation, as expected for specular cylindrical structures extending outward from a stably spinning body. This leads to the conclusion that the IMAGE satellite has maintained a stable spinning attitude (as opposed to going into a chaotic tumble, for instance) throughout the observation period after loss of telemetry. If not, the glinting antennas would not show the regular temporal and spatial structure apparent in the AEOS images. The imagery in Figure 2 also shows that two of the antennas have been truncated in length since their original deployment and that one is completely missing. This confirms through remote observation the long-known status of these RPI antennas to IMAGE satellite flight engineers: on 2000-Oct-03 approximately 130 m of the antenna along

the spacecraft $-X$ axis was lost probably to micro-meteoroid or orbital debris impact; on 2001-Sep-18 roughly 25 m of the $+X$ axis was lost; on 2001-Oct-13 part of the $-Y$ antenna was lost (approximately 100 m as estimated from the images in Figure 8); and on 2002-Aug-11 most or all the $+Y$ antenna was lost [1]. Remarkably, despite these losses the RPI instrument remained scientifically productive throughout the lifetime of the IMAGE satellite.

The glinting antennas shown in Figure 1 create large-amplitude periodic variations in the measured flux of the satellite. Figures 3 through 6 show plots of the calibrated I-band stellar magnitudes for the four AEOS observations, along with illustrations of the satellite ground track as the satellite passed over Maui. The I-band magnitudes plotted in Figures 3–6 have been range normalized to account for the $1/R^2$ effects of observatory-to-object range variations as well as Sun-to-object range variations. All magnitudes reported here have been normalized to an object range of 1000 km and a solar range of one astronomical unit (AU). Each of the four photometric signatures clearly shows periodic variations with amplitudes often exceeding 1 magnitude superimposed on longer term upward, downward, or curved trends.

4 PHOTOMETRIC SIGNATURE PERIODIC ANALYSIS

Periodic analysis of the photometric variations using methods commonly applied to astronomical data [10, 11] indicates characteristic full-cycle repetition periods close to, but not exactly equal to, the rotation period of 126.066 ± 0.003 seconds indicated in the last down-linked telemetry from the satellite. A more detailed analysis of the AEOS data, however, indicates that the measured periods vary significantly during each of the four individual observations, and that these variations reflect the distinction between “synodic” (or apparent) periodicities versus “sidereal” (or actual) rotation rates. The distinction between synodic and sidereal periods has been discussed in detail by the asteroid observational community (see [12, 13] and references therein). Synodic periods are measured quantities, and can be influenced by the relative motion of the satellite, observer, and illumination source. For instance, if a spinning body moves quickly with respect to an observer, the apparent rotation rate *as seen from the observer’s perspective* can deviate significantly from the actual rotation rate of the body. An extreme example in this respect is the Moon, which always presents the same face to the Earth showing no *apparent* rotation even though it is actually rotating once every 28 days. In order to evaluate the actual spin rates of the IMAGE satellite using the AEOS time-resolved photometry, two analyses are required. First, the photometric data must be analyzed to determine accurate synodic modulation periods. Second, the synodic periods must be converted to sidereal rotation periods by accounting for the effects of the relative motion of the satellite, observatory, and illumination source during the observations.

4.1 Fourier-series Method to Determine Synodic Periods

Following the method suggested in ref. [12], we have developed and applied a Fourier-series-based analysis to determine synodic periods from the AEOS time-resolved photometric data. This entails modeling the fluxes observed during a specified time interval with a series of the form:

$$F'(t) = \left[\sum_{m=0}^M a_m t^m \right] + \left[\sum_{n=1}^N b_n \cos(n\omega t) + c_n \sin(n\omega t) \right] \quad (1)$$

The first polynomial series allows the reproduction of long term non-periodic trends in flux and the second Fourier series allows reproduction of superimposed periodic variations, both of which are observed in the AEOS VisIm observations (see the middle panels of Figures 3–6). Equation (1) contains a total of $M+2N+2$ unknown parameters: $M+1$ polynomial series coefficients (a_m), a total of $2N$ Fourier series coefficients (b_n, c_n), and one Fourier frequency, ω . As explained below, a least-squares analysis provides the means to determine these unknown parameters and generate a best-fit to the data.

A model of the i^{th} measured flux can be expressed by averaging the flux given in equation (1) over the CCD exposure time:

$$F'_i = \frac{1}{\tau_i} \int_{t_i}^{t_i + \tau_i} [F'(t)] dt \quad (2)$$

where t_i denotes the time at the beginning of the exposure and τ_i denotes the exposure time. This model flux provides the means to write the least-squares chi-squared metric:

$$\chi_F^2 = \sum_i \left(\frac{F_i - F'_i}{\Delta F_i} \right)^2 \quad (3)$$

where F_i denotes the observed fluxes and ΔF_i the associated measurement uncertainties. Minimizing this function with respect to the $M+2N+2$ unknown parameters yields the best-fit to the data. Fortunately, the best-fit $M+2N+1$ series coefficients (i.e., a_m , b_n , c_n) can be found efficiently using linear matrix methods [14], leaving only the frequency parameter ω to be found using non-linear methods.

This Fourier-series based least-squares procedure provides a robust estimate of the characteristic frequency of modulation even in the presence of significant long-term trends and it has the capability to model variations in flux occurring on timescales shorter than the observation exposure times, given observations of sufficient quality. The best-fit frequency ω calculated using this procedure can be used to derive the corresponding synodic period, $T_{SYN} = 2\pi / \omega$.

4.2 Measured Synodic Periods for the IMAGE Satellite

The Fourier-series periodic analysis method provides a means to measure variations in synodic period during the AEOS VisIm photometric observations of the IMAGE satellite shown in Figures 3–6. The adopted method employs a “sliding-window” technique, where multiple least-squares analyses were performed sequentially for a series of time “windows” spanning the observations. For the IMAGE data, the procedure employed a quadratic polynomial series ($M=2$), a total of 30 Fourier terms ($N=15$) and a window width of $w = 252$ s (approximately two rotation periods). The analysis proceeded as follows:

- 1) For a given time, t , find all photometric measurement measurements within the time-window interval $t-w/2$ to $t+w/2$;
- 2) perform a least-squares Fourier-series analysis to determine the best-fit synodic period for that interval; and
- 3) increment the time and repeat the procedure “sliding” the window across the entire set of observations.

The bottom panels in Figures 3–6 show the best-fit synodic periods generated using this procedure, plotted on the same time-axis scale as the photometric data shown directly above. The analysis indicates significant variations in synodic periods between about 121 s and 127 s during the four observations.

5 SPIN STATE ANALYSIS USING TIME-RESOLVED PHOTOMETRY

As discussed earlier, converting synodic periods (or frequencies) into sidereal values requires accounting for the relative motion of the observatory, the satellite, and the Sun, and has been discussed in detail by the asteroid observation community [12, 13]. The synodic/sidereal difference depends on the spin axis orientation of the spinning body. In fact, using an analysis procedure called the “epoch method” [13], well-observed variations in synodic frequencies can be used to derive complete spin state solutions, yielding both spin axis orientation and sidereal rotation rates of the observed object. Although developed for asteroid characterization, the method applies equally well to artificial satellite observations because it is independent of the shape and reflectivity characteristics of the observed object. (An alternate method applied to asteroids for spin state determination called the “amplitude method” is not as well suited for artificial satellite observations because it relies more on the nearly ellipsoidal shapes and diffuse reflectivity characteristics of asteroids).

5.1 The Epoch Method of Spin State Determination

Asteroid researchers developed the epoch method for determining the spin state of non-resolved objects observed in reflected sunlight using time-resolved photometry (see [12, 13] and references therein). The

epoch method formulation employs a set of measured synodic frequencies to determine a rotating object's sidereal angular spin rate, Ω , and spin axis orientation. The spin axis can be specified by RA/DEC angles (α , δ) or, alternatively, Euler angles [4] given by $\phi = 90^\circ + \alpha$ and $\theta = 90^\circ - \delta$. The sidereal spin rate is typically reported in terms of frequency of revolution, $\nu = \Omega / 2\pi$ (often in units of rpm). The sidereal period is given by $T_{SID} = 2\pi / \Omega$. Generally, researchers have applied the epoch method to observations acquired over time scales sufficiently short so that temporal changes in the three parameters that specify the spin state (Ω, ϕ, θ) can be neglected, although this should be justified *post facto*.

The epoch method relies on the two fundamental assumptions: 1) that the observed body is in a stable spin rotational state, and 2) that each full-cycle synodic period measured by the observer corresponds to the time interval required for the body to rotate such that the “phase angle bisector” makes one complete revolution in azimuthal angle around the spin axis, as discussed in more detail below [13]. Most asteroids satisfy the first assumption rigorously because their rotational motions have relaxed over very long time scales into stable, principal-axis spin states [12]. Spin-stabilized spacecraft also satisfy the first assumption by design. However, if attitude control is lost, such spacecraft can potentially evolve into unstable or chaotic rotational states depending on the characteristics of their inertia tensor and the presence of environmental torques [4]. The phase angle bisector (PAB) is the direction midway between the body-to-observer and body-to-Sun direction vectors. Over short time scales, corresponding to small changes in observation and solar illumination angles, the single-cycle reflected-light signature of a spinning body is controlled to a large extent (but not entirely) by the position of the PAB with respect to the body's spin axis, providing the basis of the second assumption employed in the epoch method.

5.2 The Phase-Angle Bisector and the Relation Between Synodic and Sidereal Frequency

In the Earth-centered inertial (ECI) reference frame, denoted here by the “*” superscript, the PAB unit vector can be expressed as

$$\hat{\mathbf{b}}^*(t) = \frac{\hat{\mathbf{o}}^* + \hat{\mathbf{s}}^*}{|\hat{\mathbf{o}}^* + \hat{\mathbf{s}}^*|} \quad (4)$$

where $\hat{\mathbf{o}}^*$ and $\hat{\mathbf{s}}^*$ denote the ECI-frame body-to-observer and body-to-Sun direction unit vectors. In general, the PAB unit vector varies as a function of time. This vector can be transformed into the “spin axis reference frame” which has its z-axis directed along the spin axis, and its x- and y-axes fixed in the ECI frame (see [4]):

$$\hat{\mathbf{b}}(t, \phi, \theta) = [\mathbf{R}(\phi, \theta)] \hat{\mathbf{b}}^*(t) \quad (5)$$

where the 3×3 rotation matrix, \mathbf{R} , depends on the spin axis Euler angles as follows:

$$\mathbf{R}(\phi, \theta) = \begin{bmatrix} 1 & 0 & 0 \\ 0 & \cos \theta & \sin \theta \\ 0 & -\sin \theta & \cos \theta \end{bmatrix} \begin{bmatrix} \cos \phi & \sin \phi & 0 \\ -\sin \phi & \cos \phi & 0 \\ 0 & 0 & 1 \end{bmatrix} \quad (6)$$

The PAB azimuthal and axial angles (Ψ , Θ) relate to the unit vector given in equation (5) as follows:

$$\hat{\mathbf{b}} = \begin{bmatrix} \cos \Psi \sin \Theta \\ \sin \Psi \sin \Theta \\ \cos \Theta \end{bmatrix} \quad (7)$$

Equations (4)–(7) provide the means to derive the PAB azimuthal angle as a function of time and spin axis orientation, $\Psi = \Psi(t, \phi, \theta)$.

The epoch method assumes that azimuthal motion of the PAB (i.e., temporal changes in Ψ) creates the difference between synodic and sidereal frequencies [13], leading to the following expression for the expected (or model) synodic frequency at a particular time given the three spin state parameters (Ω, ϕ, θ):

$$\omega'(t, \Omega, \phi, \theta) = \Omega - \frac{\partial \Psi(t, \phi, \theta)}{\partial t} \quad (8)$$

To model a specific measurement of the synodic frequency ω_i averaged over a window $t_i - w/2 \leq t \leq t_i + w/2$ (as described in section 4.2 above) equation (8) can be integrated in time

$$\omega'_i(\Omega, \phi, \theta) = \Omega - \left[\int_{t_i - w/2}^{t_i + w/2} \frac{\partial \Psi(t, \phi, \theta)}{\partial t} dt \right] \approx \Omega - \left[\frac{\Psi(t_i + w/2, \phi, \theta) - \Psi(t_i - w/2, \phi, \theta)}{w} \right] \quad (9)$$

where the second expression is applicable over time windows short enough to ensure that the two terms in the square brackets are approximately equal (i.e., their difference must be small compared to $\Delta\omega_i$, the measurement uncertainty on ω_i).

5.3 Least-squares Spin State Determination

The epoch method of determining an object's spin state from measured synodic frequencies can be formulated as a least-squares problem. Given a time-series of measured synodic frequencies (t_i, ω_i), such as those plotted in the bottom panels of Figures 3–6, the epoch method goodness-of-fit indicator may be defined as follows:

$$\chi_\omega^2 = \chi_\omega^2(\Omega, \phi, \theta) = \sum_i \left(\frac{\omega_i - \omega'_i(\Omega, \phi, \theta)}{\Delta\omega_i} \right)^2 \quad (10)$$

where $\Delta\omega_i$ denotes the uncertainty on the measured frequency and ω'_i and denotes the model synodic frequency given by equation (9). Determining the best-fit spin state requires minimizing this function with respect to the three parameters (Ω, ϕ, θ). Fortunately, the best-fit sidereal frequency can be found analytically by solving the equation

$$\left(\frac{\partial [\chi_\omega^2(\Omega, \phi, \theta)]}{\partial \Omega} \right)_{\Omega_0} = 0 \quad (11)$$

which yields the following expression

$$\Omega_0 = \Omega_0(\phi, \theta) = \frac{\sum_i W_i (\omega_i + \dot{\Psi}_i(\phi, \theta))}{\sum_i W_i} \quad (12)$$

where $W_i \equiv \Delta\omega_i^{-2}$ and $\dot{\Psi}_i(\phi, \theta)$ is the quantity given in square brackets in equation (9). This best-fit frequency can be inserted into the goodness-of-fit indicator from equation (10) to define a new indicator as follows:

$$\chi_0^2(\phi, \theta) = \chi_\omega^2(\Omega_0, \phi, \theta) \quad (13)$$

The best-fit spin axis can be found by minimizing this quantity with respect to (ϕ, θ) . Because of the highly non-linear nature of this 2-dimensional function, this procedure does not lend itself to a straightforward analytical solution but can be calculated numerically relatively efficiently even for large data sets. Our analysis employs a grid-search at fine increments over the entire (ϕ, θ) domain, followed by a simplex non-linear numerical minimization procedure to home-in on the best-fit angles [14].

6 IMAGE SATELLITE SPIN STATE ANALYSIS

The last telemetry from the IMAGE satellite attitude control system on 2005-DEC-12 [3] indicated a sidereal spin rate of $\nu = (0.47594 \pm 0.00012)$ rpm and spin axis angles $\phi = (21.8 \pm 1.4)^\circ$ and $\theta = (90.7 \pm 1.4)^\circ$. Applying the epoch method analysis procedure to the four AEOS measurements yields best-fit spin axis angles consistent with these telemetry values to within statistical uncertainty. However, best-fit spin rates show a statistically significant declining trend during the 170-day period following loss of telemetry, despite intervening attempts by ground-controllers to command an increase in spin rate.

6.1 IMAGE Spin Axis Determination from AEOS Photometric Data

Table 1 lists spin state parameters for the image satellite. The first entry in Table 1 shows parameters taken from the last down-linked quaternion telemetry. The second entry shows the best-fit parameters from the epoch-method analysis applied to the combined data from AEOS observations conducted 2006-028, -031 and -034; Figure 7 shows the corresponding gray-scale plot of the goodness-of-fit indicator from equation (13) as a function of the spin axis angles ϕ and θ . The analysis yields best-fit axis angles of $\phi = (17.9 \pm 4.4)^\circ$ and $\theta = (88.7 \pm 3.9)^\circ$, within statistical uncertainty of those last down-linked from the satellite. Table 1 also shows the best-fit spin state parameters derived from these three AEOS data sets analyzed individually (entries 3–5), as well as the best-fit parameters from the AEOS data from 2006-150 (entry 6). Notably, even the 2006-150 observation indicates the same axis orientation to within statistical uncertainty, implying that the spin axis remained stable to within detection limits during the 170-day period after loss of telemetry.

Table 1. IMAGE Satellite Spin State Parameters

Entry	Year	DOY Range	ϕ (degrees)	θ (degrees)	ν (rpm)
1	2005	346.25 – 346.32	$21.8 \pm 1.4^*$	$90.7 \pm 1.4^*$	$0.47594 \pm 0.00012^*$
2	2006	028.66 – 034.61	$17.9 \pm 4.4^\#$	$88.7 \pm 3.9^\#$	$0.47452 \pm 0.00041^\#$
3	2006	028.66 – 028.68	16.9 ± 5.4	90.4 ± 8.4	0.47472 ± 0.00051
4	2006	031.62 – 031.65	17.1 ± 4.5	89.8 ± 2.4	0.47462 ± 0.00051
5	2006	034.59 – 034.61	20.4 ± 4.5	81.7 ± 2.5	0.47457 ± 0.00029
6	2006	150.23 – 150.25	23.1 ± 4.4	89.2 ± 3.9	0.47138 ± 0.00035
7	2006	028.66 – 028.68	$21.8 \pm 1.4^*$	$90.7 \pm 1.4^*$	0.47435 ± 0.00059
8	2006	031.62 – 031.65	$21.8 \pm 1.4^*$	$90.7 \pm 1.4^*$	0.47412 ± 0.00059
9	2006	034.59 – 034.61	$21.8 \pm 1.4^*$	$90.7 \pm 1.4^*$	0.47413 ± 0.00040
10	2006	150.23 – 150.25	$21.8 \pm 1.4^*$	$90.7 \pm 1.4^*$	0.47094 ± 0.00042

*Parameters taken from last down-linked IMAGE satellite quaternion telemetry [3].

[#]Parameters determined by combining three AEOS observations conducted on 2006-028, -031, and -034.

6.2 IMAGE Spin Rate Determination from AEOS Photometric Data

Because of the implied axis orientation stability, entries 7–10 of Table 1 list best-fit spin rates derived using the last down-linked spin axis parameters directly in equation (12), instead of finding best-fit values for (ϕ, θ) . Figure 8 shows the corresponding synodic periods, indicating that the models reproduce the observations exceedingly well. The derived sidereal spin rates listed in Table 1 clearly show a declining trend. Notably, AEOS measured a significant decline between the observations conducted on 2006-034 and 2006-150, which is especially significant because IMAGE flight engineers attempted to up-link

commands to the spacecraft during this period to increase the satellite’s spin rate. Specifically, on 2006-047 (Feb. 16) and again on 2006-061 (Mar. 2) commands were issued to increase to a target rate of 0.52 rpm [3]. The AEOS data clearly indicate that the spacecraft failed to receive and/or execute these up-linked commands.

Figure 9 shows a plot of the steadily declining spin rate of the IMAGE satellite. The five plotted points comprise the last down-linked spin rate (Table 1, entry 1) and the four AEOS-measured spin rates (Table 1, entries 7–10). These data can be fit using an exponentially decaying model expected for a satellite experiencing a dampening torque, such as that arising from magnetically induced currents (c.f., [15]):

$$v(t) = v(t_0) e^{-(t-t_0)/\tau} \quad (14)$$

The best-fit, shown as the dotted line in Figure 9, has a decay time constant of $\tau = 41 \pm 3$ years corresponding to a spin-down rate of $(3.1 \pm 0.3) \times 10^{-5}$ rpm/day during the 170-day span of the data. This decay rate seems to exceed by a factor of ≈ 3 the spin-down rate experienced by the spacecraft during its last two years of operation [3] — an as-yet unexplained discrepancy.

7 CONCLUSIONS

The following conclusions can be drawn from the analysis of AEOS telescope observations of NASA’s IMAGE satellite:

1. The IMAGE satellite maintained a stable spin axis for at least 170 days after loss of telemetry. If this were not the case, the glinting radial antennas would not show the regular temporal and spatial structure apparent in the AEOS VisIm images, and the photometric spin state determinations would not consistently yield best-fit spin axis angles within statistical uncertainty of those last down-linked from the spacecraft.
2. The remote AEOS imagery confirms the known status of the IMAGE satellite RPI radial wire antennas: that ≈ 130 m of $-X$ antenna, ≈ 25 m of the $+X$ antenna, ≈ 100 m of the $-Y$ antenna and most of the $+Y$ antenna has been lost since the original deployment.
3. The spacecraft spin rate declined steadily during the 170 days after loss of telemetry at a rate of $(3.1 \pm 0.3) \times 10^{-5}$ rpm/day, approximately three times faster than the decay rate observed during the last two years of active satellite operation.
4. The attempts by IMAGE flight controllers to command an increase in spin rate to 0.52 rpm (up-linked on 2006 Feb 16 and again Mar 2) did not have the intended effect, implying that the spacecraft has lost the ability to receive and/or execute such commands.
5. AEOS LWIR measurements of figure-averaged radiometric temperatures proved difficult for the IMAGE spacecraft engineering team to use for remote characterization because of the relatively small expected difference in the thermal signature of the spacecraft in nominal operational mode versus safe mode.

8 FIGURES

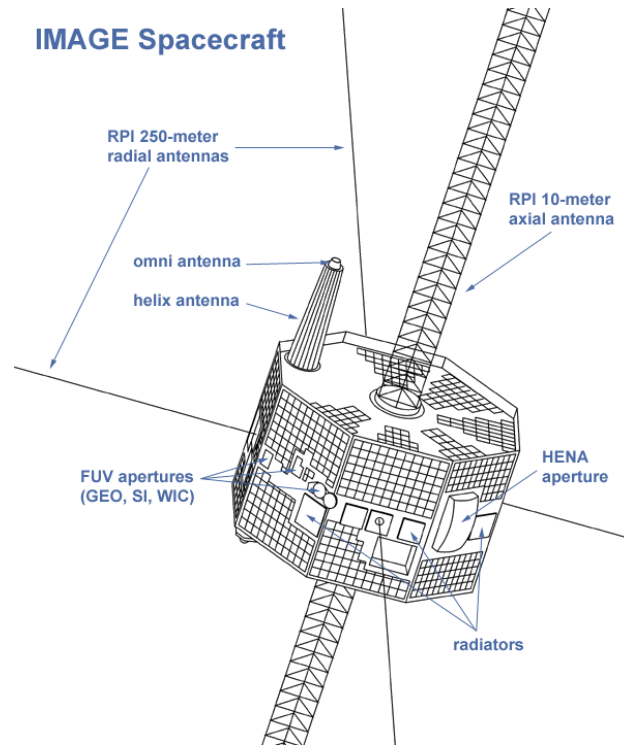


Fig 1. A schematic illustration of the IMAGE spacecraft [3] including the octagonal central bus, the triangular axial antennas extending parallel to the spin axis, and portions of the four radial wire antennas that originally extended 250 meters outward from the spacecraft equator. The ≈ 0.5 -rpm spin of the spacecraft keeps these four wire-thin radial antennas extended outward under tension. During operation, the spacecraft's attitude control system maintained the spin axis in an orientation perpendicular to the orbital plane.

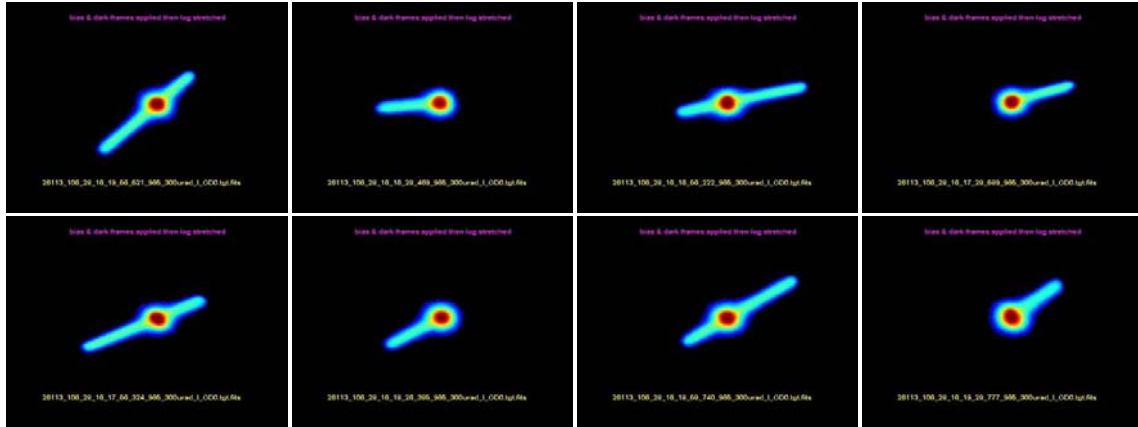


Fig. 2. Eight AEOS VISIM wide field-of-view images of NASA's IMAGE satellite showing the radial wire antennas glinting in reflected sunlight. These false-color images were acquired 2006-028 when the observatory-to-spacecraft range was between 2,500 and 3,050 km. The images show almost two complete satellite rotations (from top-left to top-right and bottom-left to bottom-right) each separated by one-quarter of a rotation period (approximately 30 seconds). The first (top-left) image shows the +X antenna extending to the lower left of the central body, and the -X antenna extending to the upper right, confirming that the -X antenna has lost about 130 m of its original 250 m length. The second image acquired approximately $\frac{1}{4}$ of a rotation later shows a slightly truncated -Y antenna extending to the left of the central body, but with no antenna extending on the opposite side of the central body, confirming that the +Y antenna is completely missing. The third image shows the $\pm X$ antennas again, but on opposite sides of the central body than in the first image, as expected after $\frac{1}{2}$ of a satellite rotation. Similarly the fourth image shows the -Y antenna again, but on the opposite side of the central body than in the second image. The second row shows that this same pattern is repeated in the immediately-following satellite rotation. The zenith (+EL) direction is upward in all of these images, explaining the slightly changing aspect angle of the antennas from frame to frame.

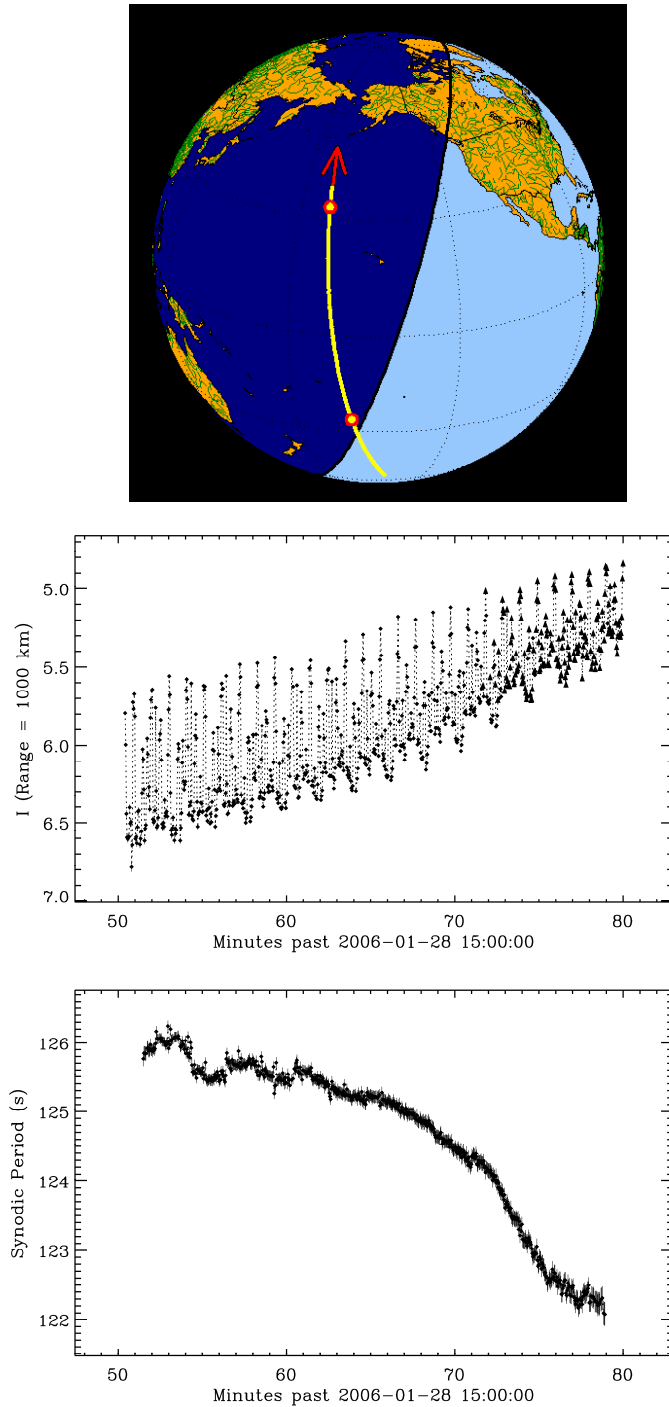


Fig. 3. AEOS VisIm photometric observation of the IMAGE satellite, conducted on 2006-028 (Jan 28). The top panel shows the ground-track of the satellite as it passed over Maui with the red circles indicating the signal acquisition and loss points. The middle panel shows the I-band stellar magnitudes as a function of time normalized to remove object and solar range variations (upward-pointing triangles indicate saturated measurements and diamonds indicate unsaturated data). Periodic variations from the spinning satellite are clearly evident in the middle panel, superimposed on a brightening trend. The bottom panel shows synodic periods derived from the time-resolved photometric data using a sliding-window Fourier analysis, indicating that full-cycle modulation periods decrease from 126 s to 122 s during the observation.

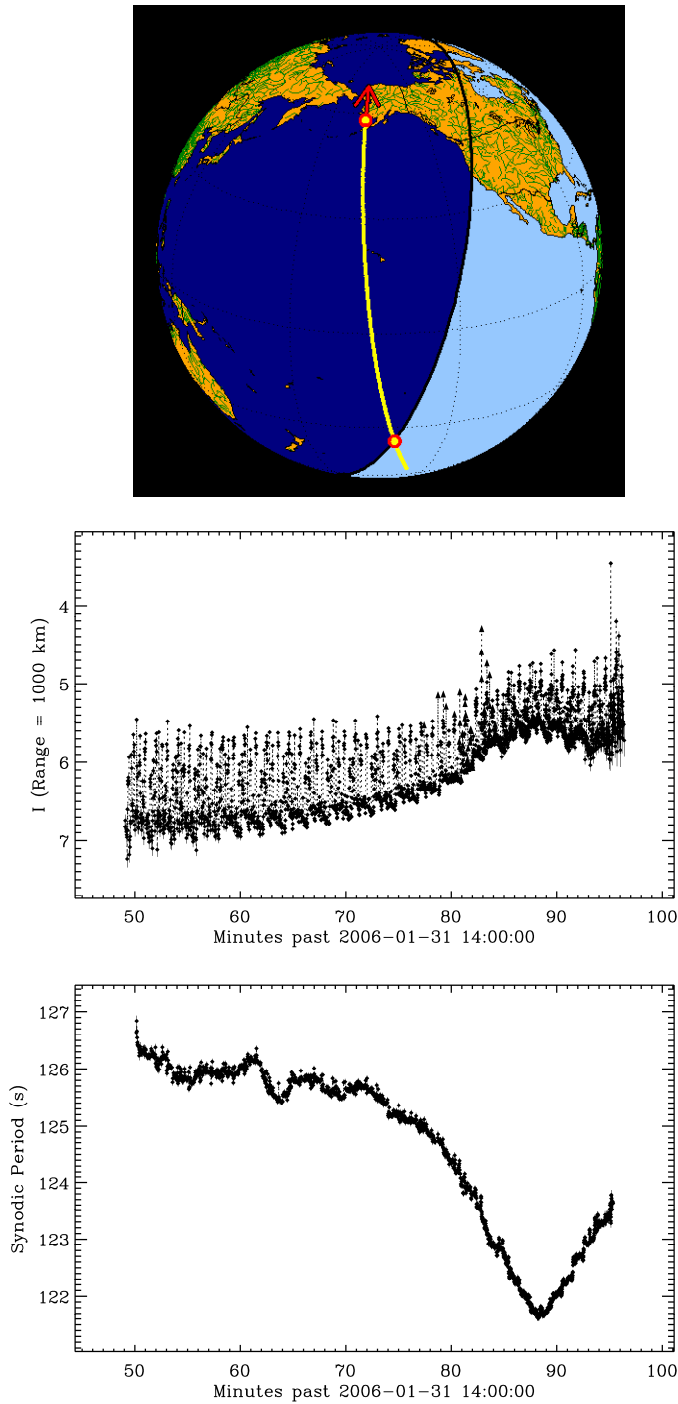


Fig. 4. AEOS VisIm I-band photometric observation of the IMAGE satellite conducted on 2006-031 (Jan 31). The top panel shows the ground-track of the satellite with the red circles indicating the signal acquisition and loss points and the arrow indicating the direction of motion. The middle panel shows the range-normalized I-band stellar magnitudes measured as a function of time, with clearly evident periodic variations from the spinning satellite superimposed on longer term temporal variations. The bottom panel shows synodic periods derived from the time-resolved brightness data using a sliding-window Fourier analysis, indicating that full-cycle modulation periods vary between 121.6 s and 126.5 s during the observation.

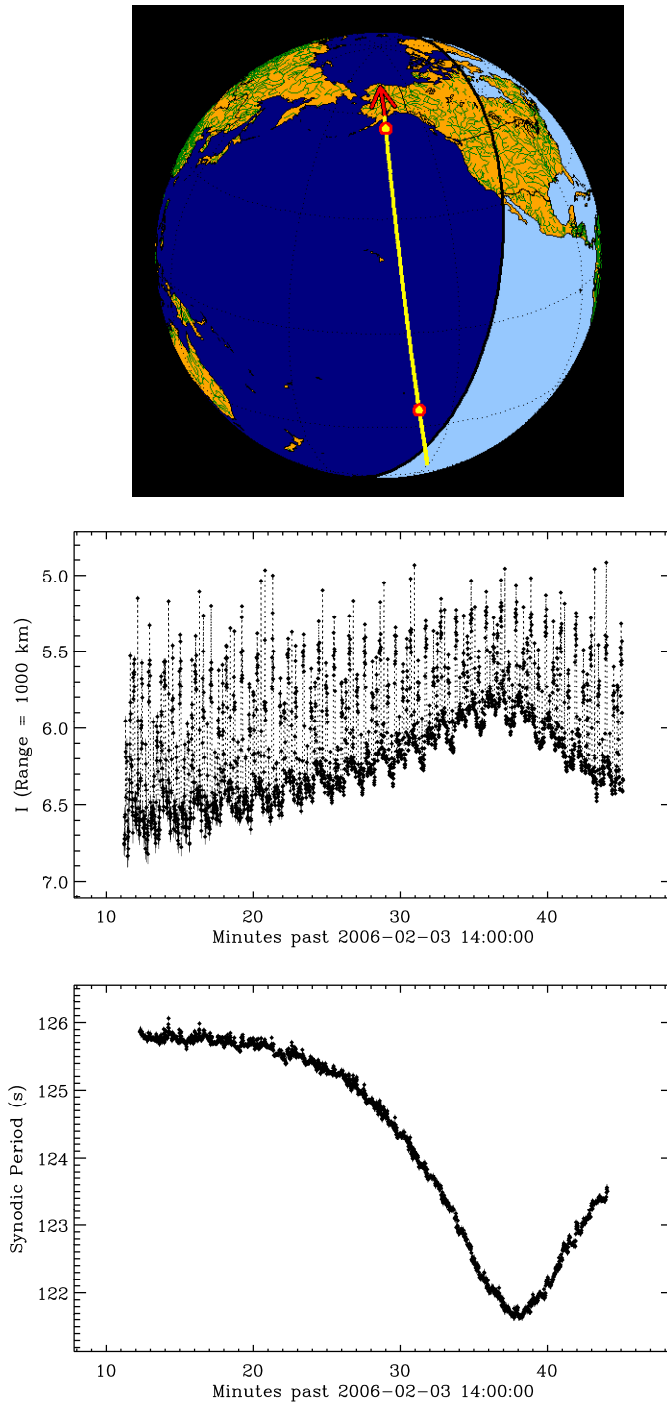


Fig. 5. AEOS VisIm I-band photometric observation of the IMAGE satellite conducted on 2006-034 (Feb 03). The top panel shows the ground-track of the satellite with the red circles indicating the signal acquisition and loss points and the arrow indicating the direction of motion. The middle panel shows the range-normalized I-band stellar magnitudes measured as a function of time, with clearly evident periodic variations from the spinning satellite superimposed on longer term temporal variations. The bottom panel shows synodic periods derived from the time-resolved brightness data using a sliding-window Fourier analysis, indicating that full-cycle modulation periods vary between 121.6 s and 125.8 s during the observation.

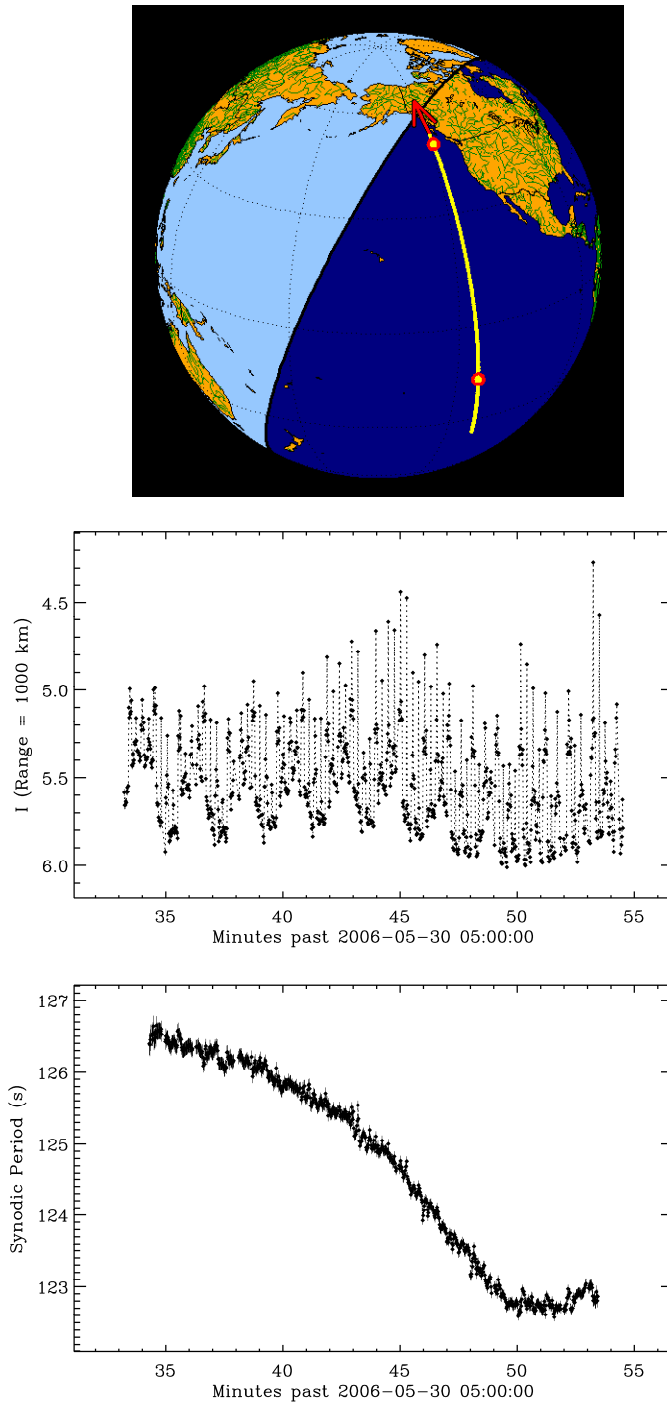


Fig. 6. AEOS VisIm I-band photometric observation of the IMAGE satellite conducted on 2006-150 (May 30). The top panel shows the ground-track of the satellite with the red circles indicating the signal acquisition and loss points and the arrow indicating the direction of motion. The middle panel shows the range-normalized I-band stellar magnitudes measured as a function of time, with clearly evident periodic variations from the spinning satellite superimposed on a slight dimming trend. The bottom panel shows synodic periods derived from the time-resolved brightness data using a sliding-window Fourier analysis, indicating that full-cycle modulation periods vary between 122.7 s and 126.5 s during the observation.

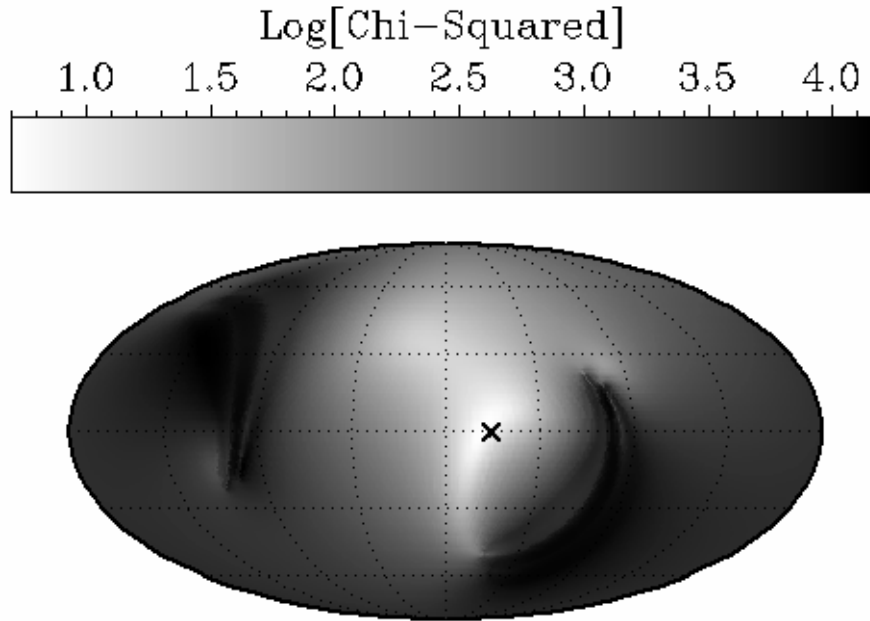


Fig. 7. Mollweide projection of the epoch method goodness-of-fit parameter as a function of IMAGE spacecraft spin axis orientation angles (ϕ , θ). This gray-scale plot of the chi-squared indicator from equation (13) shows the results of the epoch method spin state analysis applied to the combined data from the first three AEOS observations of the IMAGE satellite conducted on 2006-028, -031 and -034. The central meridian of this plot corresponds to $\phi = 0$ with ϕ increasing from left to right; the top corresponds to $\theta = 0$ and the bottom to $\theta = 180^\circ$. Lighter gray-scale regions show areas of higher quality fits to the data, and the minimization analysis yields best-fit values of $\phi = (17.9 \pm 4.4)^\circ$ and $\theta = (88.7 \pm 3.9)^\circ$. These best-fit angles are within statistical uncertainty of those last down-linked from the satellite's attitude control system, $\phi = (21.8 \pm 1.4)^\circ$ and $\theta = (90.7 \pm 1.4)^\circ$, shown as the bold \times symbol on the plot.

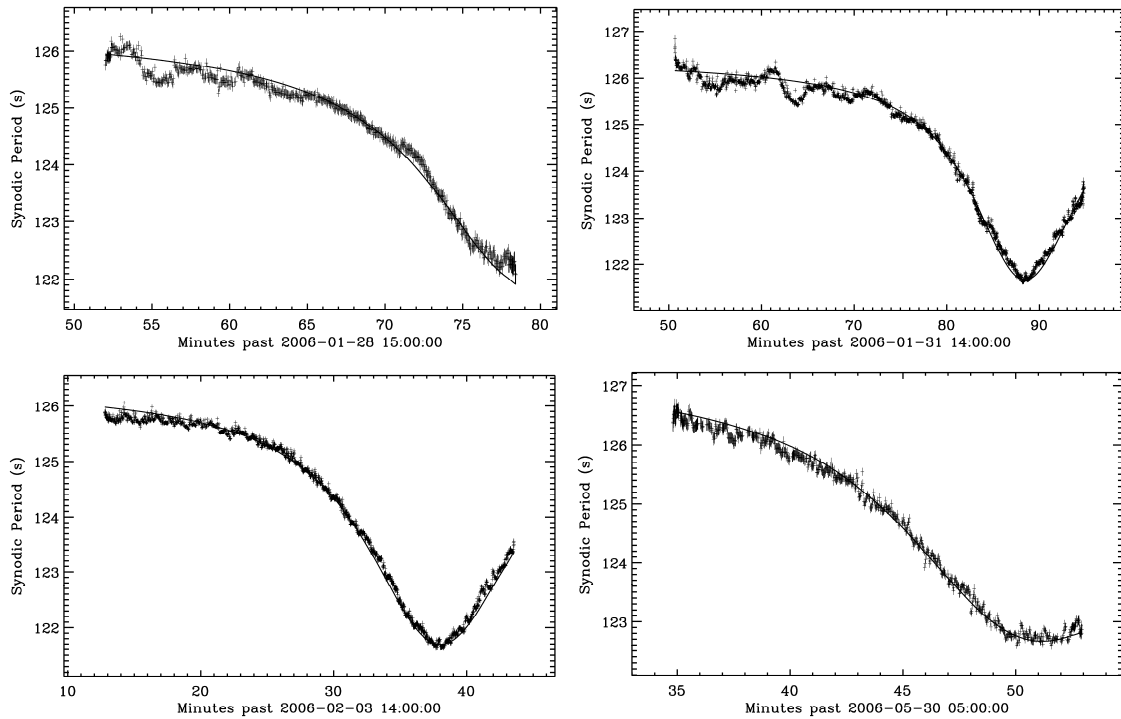


Fig. 8. Best-fit models of the measured synodic periods from AEOS observations of the IMAGE satellite. The “+” symbols show the AEOS VisIm measurements from 2006-028 (upper left), 2006-031 (upper right), 2006-034 (lower left) and 2006-150 (lower right). The solid lines on each plot indicate the best-fit model synodic periods calculated using equation (9) with the spin axis parameters last down-linked from the satellite’s attitude control system, $\phi = 21.8^\circ$ and $\theta = 90.7^\circ$. The error bars on the data show estimated measurement uncertainties (which are smaller than the plotted “+” symbols in some cases).

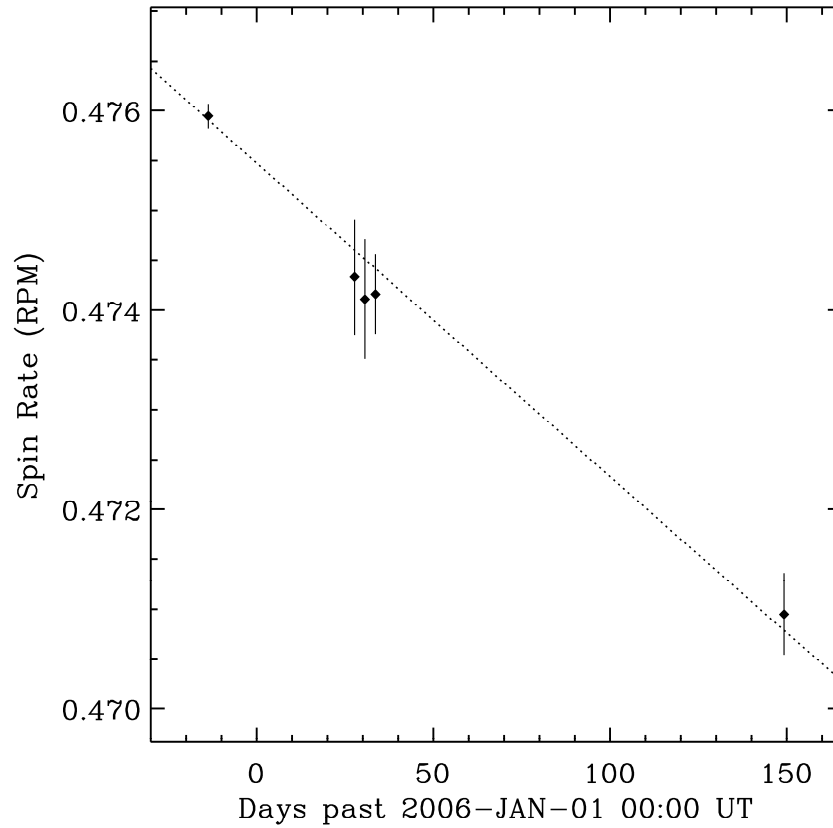


Fig. 9. Sidereal spin rates for the IMAGE satellite as a function of time (black diamond symbols) and an exponential decay model (solid line). The first data point shows the spin rate down-linked from the satellite attitude control system on 2005-Dec-12, just before loss of telemetry. The last four data points show the rates measured remotely using AEOS telescope time-resolved photometric observations. The measured spin rates show a steady declining trend, despite intervening efforts by IMAGE satellite controllers to command the spacecraft to increase its spin rate.

9 ACKNOWLEDGEMENTS

The authors would like to thank John Lambert for insightful explanations of the epoch method of determining spin states, Thomas Kececy for discussions of the dynamics of satellite spin deceleration in the presence of dampening environmental torques and the AEOS telescope operations team for executing the observation plan.

10 REFERENCES

1. See the NASA Goddard Space Flight Center IMAGE mission web site (<http://image.gsfc.nasa.gov>) and references therein for details on the mission history of the spacecraft (accessed for this work Feb – Jul 2006).
2. Gibson, W. et al., “IMAGE, the First of the New MIDEX Missions,” *13th AIAA/USU Conference on Small Satellites*, Logan, UT, 1999.
3. Prior, Michael, *Hubble Space Telescope Deputy Operations Manger*, Code 440.8, Goddard Space Flight Center, Greenbelt, MD 20771, mprior@hst.nasa.gov, private communication Jan.-July, 2006.
4. Goldstein, H., “Classical Mechanics” Addison-Wesley Pub. Co., Reading Massachusetts, 1981.
5. Hall D. et al., “AEOS I-band Photometry of Moving Targets,” *The 2003 AMOS Technical Conference Proceedings*, Kihei, HI, 2003.
6. Witte, D., “The AEOS LWIR Imager: A Tool for Space Object Thermometry,” *The 1999 AMOS Technical Conference Proceedings*, Kihei, HI, 1999.
7. Mayo, J., “AEOS 3.67 Meter Telescope Optics: Design, Fabrication, and Performance,” *The 1999 AMOS Technical Conference Proceedings*, Kihei, HI, 1999.
8. Berger, P., “AEOS Adaptive Optics System and Visible Imager,” *The 1999 AMOS Technical Conference Proceedings*, Kihei, HI, 1999.
9. Landolt, A., “UBVRI Photometric Standard Stars in the Magnitude Range $11.5 < V < 16.0$ Around the Celestial Equator,” *The Astronomical Journal*, Vol. 104, 340–49, 1992.
10. Scargle, J., “Studies in Astronomical Time Series Analysis II. Statistical Aspects of Spectral Analysis of Unevenly Spaced Data,” *The Astrophysical Journal*, Vol. 263, 834–53, 1982.
11. Larsson, S., “Parameter Estimation in Epoch Folding Analysis,” *Astron. Astrophys. Supp. Ser.*, Vol. 117, 197–201, 1996.
12. Magnusson, P., “Distribution of Spin Axes and Senses of Rotation for 20 Large Asteroids,” *Icarus*, Vol. 68, 1–39, 1986.
13. Magnusson, P. et al., “Determination of Pole Orientations and Shapes of Asteroids,” in *Asteroids II* (edited by R. Binzel et al.) 66–97, University of Arizona Press, 1989.
14. Press, W. et al., “Numerical Recipes in FORTRAN: The Art of Scientific Computing” (2nd Edition), Cambridge University Press, New York, NY, 1992.
15. Bertotti, B. and Iess, L., “The Rotation of Ligeos,” *Journal of Geophysical Res.*, Vol. 96, 2431–40, 1991.

